Interferometer Design for Attosecond Experiments

Simon Ek

Supervisor: Johan Mauritsson

Bachelor thesis, spring term, 2015

LRAP-505

LUND UNIVERSITY

Department of Physics

Atomic Physics

Interferometer Design for Attosecond Experiments

Simon Ek

Supervisor: Johan Mauritsson

Abstract

Resolving fast events, such as electron dynamics, requires short light pulses. To this date the shortest available light pulses are created using High-order Harmonic Generation (HHG) and have a duration of a few hundred attoseconds (1 as = 10^{-18} s). When used for pump-probe experiments, these pulses are generated in an interferometer, which needs to be stable for the experiment to yield high quality data.

In this project the effect of interferometer stability (seen as uncertainty in the time delay, $\Delta\tau$) on the possibility to extract a phase with high precision from data has been investigated. This was done by simulations in MATLAB. It was found that even with a large error in the time delay ($\sigma_{\Delta\tau} = 0.20T$) it is possible to extract a phase with a small error ($\sigma_\phi < 0.001T$), if the number of data points is sufficient (N =100 000).

Furthermore the effect of some aspects of interferometer design on the stability of interferometers was investigated by simulations in the ray tracing program FRED. An interferometer design was modified in one aspect at the time and the stability, in terms of spatial and temporal drift, was measured for each modification. In this way it was found that an interferometer should 1) be small, 2) have equal parity of the number of focusing lenses and mirrors, respectively, in its two arms, 3) have focusing lenses of equal focal length in its arms, and 4) have its mirrors perfectly aligned, to be as stable as possible. For short: a stable interferometer is small and symmetric.

Contents

1 Introduction **3**

2 Background **4**

2.1 The Gaussian beam 4

2.2 High-order Harmonics Generation 5

2.3 Attosecond Pulse Trains 6

2.4 Interference 7

2.5 Interferometers 7

2.6 Reconstruction of Attosecond Beating by Interference of Two-photon Transitions 8

3 Method **10**

3.1 Error propagation in a sine function 10

3.2 Stability of interferometers 11

3.2.1 The stress test 12

3.2.2 The interferometer designs 13

4 Results and discussion **15**

4.1 Sine error propagation 15

4.2 Stability of interferometers 18

4.3 The temporal drift simulations 23

4.4 Considering the Rayleigh range 23

5 Conclusions **25**

6 Outlook **25**

Acronyms

APT Attosecond Pulse Train

HHG High-order Harmonic Generation

RABITT Reconstruction of Attosecond Beating by Interference of Two-photon Transitions

1 Introduction

To resolve extremely fast events short light pulses are needed. In 2001 Paul and co-workers managed to create and for the first time measure pulses shorter than one femtosecond (1 fs = 10^{-15} s), so called attosecond (1 as = 10^{-18} s) pulses [1]. With these pulses the possibility to do attosecond time-resolved measurements opened up. Since electron dynamics take place on this time scale, the advent of attosecond pulses meant that measuring the motion of electrons in different systems was finally possible. As this new technique was developed a new field of research, attosecond physics, was established.

The attosecond group in Lund first measured attosecond pulses in 2003 [2] and has since continued to further develop the field. A typical attosecond experiment consists of the following: a pulsed high-power laser, an optical setup including a Mach–Zehnder interferometer and an electron detection system. Typically a large number of acquisitions are done in series to get a sample that can be analyzed. It is important that the setup is stable during the entire process of measuring, so that data taken at different times can be compared. Absolute stability, which would mean that the two arms of the interferometer do not drift neither spatially nor temporally compared to each other is, however, not necessary to obtain high quality data. Still, it is important to keep the drift, which is a consequence of vibrations and thermal expansion of components, at a minimum.

In a measurement series the signal strength at different time delays (from now on time delay is replaced by just delay) is measured repeatedly. Due to random temporal drifts the delay at which the individual measurement is actually performed is not known exactly. This means that when a certain delay $\Delta\tau_i$ is chosen and the signal strength is measured, it is, in reality, *not* the signal strength at this particular delay $\Delta\tau_i$ that is measured, but the signal strength at $\Delta\tau_i + \delta_\tau$, for some small error δ_τ. The error in delay will lead to the introduction of an error in the measured signal strength, which will propagate to the phase shift ϕ that is extracted from the data. To minimize the error in delay is therefore to minimize the error in phase shift. This can be done by using an interferometer that is as stable as possible, or by monitoring the drift and compensating for it in real time.

The aim of this project is to optimize the stability of interferometers designed for attosecond experiments. To reach this goal two main questions need to be answered. The first is: how do errors in individual measurements of intensity propagate to the extracted phase? The answer to this question should address whether the sampling method matters, how the number of individual measurements affects the size of the error in the phase and how big the error in delay can be without making it impossible to find the phase. In particular this question concerns what sufficient stability is. The second question concerns how sufficient stability can be achieved. The concrete question is: how can the errors in the individual measurements be minimized with respect to some aspects of interferometer design? To truly minimize the error over all possible designs is clearly not viable within this project and therefore only a few aspects of interferometer design can be investigated. These are: arm length, spanned area, mirror parity (more correctly, difference in parity of the number of mirrors between the arms), lens parity, combined lens and mirror parity, difference

in focal length of lenses, and how well mirrors are aligned. The answer to this question will help design a new interferometer system, which will be built in the near future by the attosecond group in Lund.

2 Background

In this section theoretical background to the project will be briefly explained. All attosecond physics ultimately rely on laser pulses that are shorter than one femtosecond, so the generation process of these pulses is of interest. The laser beam itself can be approximated to be a Gaussian beam and has some properties that limit how an interferometer, intended for attosecond experiments, can be built. These properties are also of interest. The interferometer that will be designed will be used for RABITT (Reconstruction of Attosecond Beating by Interference of Two-photon Transitions), a method that utilizes HHG (High-order Harmonics Generation), APT (Attosecond Pulse Trains) and interference. Also, interference will be an important tool when measuring the stability of different interferometer designs. With this in mind the subjects of the background section will be: The Gaussian beam, HHG, APT, interference, interferometers, and RABITT.

2.1 The Gaussian beam

A beam is said to be Gaussian if its intensity as a function of distance from the beam axis is described by a Gaussian distribution function. The laser beams that this project concerns can be approximated to be Gaussian.

When a Gaussian beam is being focused its minimum waist radius, W_0, depends on the wavelength, λ, and the focusing angle, θ_0, as

$$W_0 = \frac{\lambda}{\pi\theta_0}. \tag{1}$$

The focusing angle can be calculated if the focal length, f, and the beam radius at the focusing device, r, is known. If the focal length is much larger than the beam radius, then

$$\theta_0 = arctan\frac{r}{f} \approx \frac{r}{f}. \tag{2}$$

The waist size, W, at distance z from the focus at $z = 0$, is given by the relation

$$W(z) = W_0\sqrt{1 + \left(\frac{z}{z_0}\right)^2},$$

where z_0 is called the Rayleigh range and is defined by

$$W(z = z_0) = \sqrt{2}W_0, z_0 > 0,$$

and can be calculated as

$$z_0 = \frac{\pi W_0^2}{\lambda} = \frac{\lambda}{\pi\theta_0^2} = \frac{\lambda}{\pi}\left(\frac{f}{r}\right)^2. \tag{3}$$

The geometry of a Gaussian beam focus can be seen in figure 1.

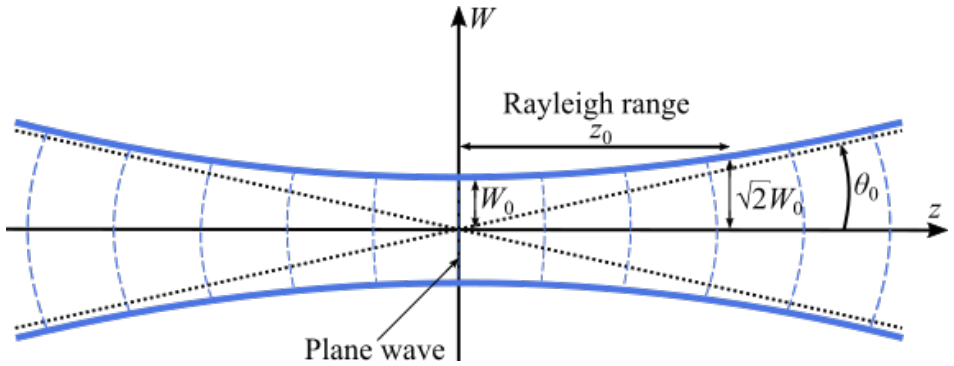

Figure 1: The geometry of a Gaussian beam focus. The solid blue line represents the border of the actual beam, and the dotted black line is the geometric approximation of the beam.

The Rayleigh range is important mainly for two reasons. First of all it is a measure of how long the focus is. Secondly it is important because the phase of a beam changes by π over a focus, and half of this change of phase takes place within the interval $[z = -z_0, z = z_0]$. This is called the Gouy effect. [3, pp. 77-81].

2.2 High-order Harmonics Generation

A problem when trying to create a short light pulse is that short pulses must have a broad bandwidth, according to the relation

$$\tau \Delta\omega \geq 1,$$

where $\Delta\omega$ is the bandwidth and τ is the duration [3, p. 1125-1126]. HHG provide a mean to obtain a coherent pulse with very broad bandwidth, and was the method used by Paul *et al.* to generate attosecond pulses. [1]

By focusing a high intensity laser pulse of frequency ω into a gas-jet, high-order harmonics of frequency $q\omega$ is created. For symmetry reasons the attosecond pulse will only consist of odd harmonics of the initial frequency, *i. e.* q is an odd integer. The initial laser frequency typically lies in the infrared (IR) part of the spectrum, while the harmonics will stretch all the way up to the region of extreme ultraviolet (XUV), and beyond.

The generation of high-order harmonics from an initial frequency can be explained by the semiclassical three-step model [4, 5]. When an atom is exposed to a high intensity ($> 10^{13} W/cm^2$) laser field, the electric component of the field will greatly influence the electric potential that binds the electrons to the atom. The first step is when the atom is ionized when an electron tunnel through the deformed potential. In step two the electron is accelerated by the electric part of the laser field, thereby gaining kinetic energy. In the third and last step the electric field changes sign and drives the electron back to its parent nuclei. If the electron recombines the kinetic energy it has gained will be released as a photon. The three-step model is illustrated in figure 2.

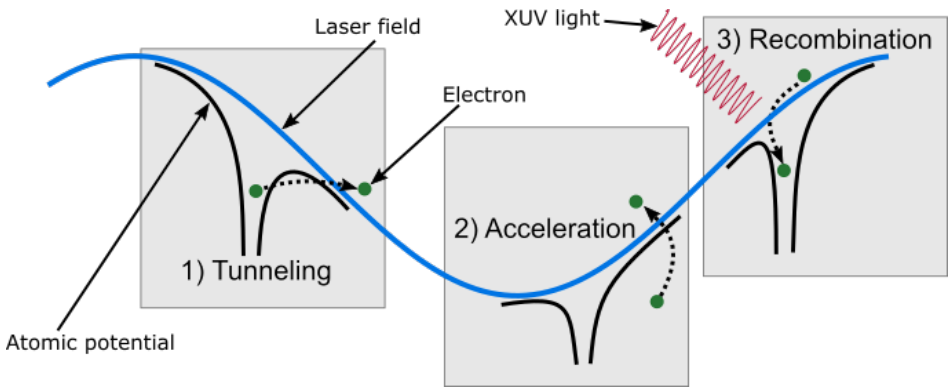

Figure 2: The three-step model of HHG. The atomic potential is altered by an intense laser field, so that an electron 1) tunnel through the potential, 2) is accelerated by the laser field, and 3) recombine.

The energy of the emitted photon depend on when during the phase of the IR field the electron tunneled out and is confined to an energy interval $I_E = [\hbar\omega_{min}, \hbar\omega_{max}]$. This means that photons of different energy will not only be separated with respect to frequency, but also with respect to time. The resulting light pulse is said to be chirped. The first half of the light pulse is up-chirped, which means that the frequency increases with time, while the last half is down-chirped, which means that the frequency decreases with time. Photons of frequencies corresponding to all energies in the interval I_E will be emitted. Since the process is repeated every time the electric field is strong enough, *i. e.* twice per period T, the odd harmonics will be amplified and all other frequencies will be extinguished. That this is the case can be seen if two consecutive emission events, each with frequency $q\omega$, is considered. The resulting electric field of these events will be

$$\begin{aligned} E(t) &= \hat{E}(t)e^{-iq\omega t} + \hat{E}(t+T/2)e^{-iq\omega(t+T/2)} \\ &= \hat{E}(t)e^{-iq\omega t}(1 - e^{-iq\omega T/2}) \\ &= \hat{E}(t)e^{-iq\omega t}(1 - e^{-iq\pi}), \end{aligned}$$

where $\hat{E}(t+T/2) = -\hat{E}(t)$ and $\omega T = 2\pi$ has been used. The absolute value of this expression will be minimized (zero) for even q's and maximized for odd q's. As the emission event is repeated a large number of times only frequencies that are close to the odd harmonics of the initial frequency will remain, *i. e.* the spectral width of the odd harmonics peaks will decrease as the number of events increase. [6, pp. 7-11]

2.3 Attosecond Pulse Trains

When an intense laser is focused at a gas the process of HHG will repeat itself as long as the intensity of the laser is sufficiently high and the gas is not completely ionized. This means that for every $T/2$ there will be a short light burst. Together these light bursts constitute an APT. As the number of HHG events N is

increased, the spectral width ν of the harmonics in the APT will decrease, since $\nu \propto \frac{1}{N}$.

In Lund a laser with a pulse duration about 35 fs and a period of 2.67 fs (corresponding to a wavelength of 800 nm) is used. This corresponds to about 10 cycles of high enough intensity to generate harmonics. The result is an APT with approximately 20 light pulses [6, p. 12]. In a new system the pulse duration will be approximately 170 fs, the period 3.43 fs (corresponding to a wavelength of 1030 nm), and therefore a number of light pulses in each APT on the order of 100.

2.4 Interference

Interference is a phenomenon where two, or more, waves are superposed. This phenomenon occurs every time more than one wave is present in the same place at the same time. The total wave function will then be the sum, that is the superposition, of the individual wave functions. This does, however, not mean that the resulting intensity will be the sum of the individual intensities. The intensity I of a wave at a certain position $\vec{x}$ is the absolute value squared of the complex amplitude U at that position $\vec{x}$. The complex amplitudes will add up to the resulting amplitude. The resulting intensity will therefore be given by

$$I = |U|^2 = \left| \sum_i U_i \right|^2 .$$

If two monochromatic lightwaves of equal frequency, the phase difference $\phi = \phi_2 - \phi_1$, and intensities I_1 and I_2 are considered, then the resulting intensity becomes

$$I = I_1 + I_2 + 2\sqrt{I_1 I_2} cos\phi. \tag{4}$$

If the amplitudes happen to be equal, such that $I_1 = I_2 = I_0$, and the phase difference is a multiple of π, $\phi = n\pi$, then eq. 4 will be zero when n is an odd integer and $4I_0$ when n is an even integer. It is clear from eq. 4 that the total intensity is dependent on the phase difference, therefore the phase difference between two light waves can be found by detecting the intensity of their superposition. This principle can be used in interferometers.[3, p. 58]

2.5 Interferometers

An interferometer, in its most basic form, works by splitting a beam of light into two arms, redirecting them by the use of mirrors, recombining them into one single beam again, and detecting the intensity of the recombined beam. The splitting and recombination of the beam can either be done by amplitude division, using a beam splitter, or by wavefront division, using a mirror with a central hole in it. Interferometers used for attosecond experiments are essentially modifications of the Mach–Zehnder interferometer, which can be seen in figure 6 in section 3.2.2.

By observing how the interference pattern at the detector changes, conclusions about the difference in optical path length between the two arms can be drawn. If, for example, the intensity changes from a

minimum to the nearest maximum at one point of the detector, then the phase difference between the arms must have changed by π, according to eq. 4. The phase difference arises because the arms are not equally long and is given by

$$\phi = 2\pi \frac{d}{\lambda}. \tag{5}$$

If ϕ changes by π, then the difference in optical path length d must have changed by $\lambda/2$. By the same reasoning it follows that if the transition from one minimum (or maximum) to the next minimum (or maximum) is repeated N times, then the optical path length has changed by $N\lambda$. [3, pp. 59-60]

2.6 Reconstruction of Attosecond Beating by Interference of Two-photon Transitions

RABITT is a method for characterizing the individual attosecond pulses in an APT, which relies on cross-correlation of adjacent harmonics [4]. This is done by focusing a generated XUV pulse and a small fraction of the fundamental IR pulse towards a gas and detecting the resulting photoelectrons. The two light pulses are phase-locked, since the XUV pulse is generated from the IR pulse at certain instants of its phase. By doing a full RABITT scan (how is described later), the relative spectral phase and amplitude of all the frequency components will be accessible, so that full reconstruction of the pulse train is possible.

When the XUV pulse, the pump, hits the gas it will ionize atoms through the photoelectric effect. Electrons will be emitted with an energy $E_q = \hbar\omega_q - I_p$ that depends on the frequency $\omega_q = q\omega$ they were ionized by, ω is the fundamental frequency of the IR pulse and I_p is the ionization potential. As the electrons reach the continuum they might, because of the presence of the IR field, either absorb or emit a photon of energy $\hbar\omega$, making it a two-photon transition in total. If this happens, the electrons will have an energy that corresponds to an even harmonic of the fundamental frequency ω. The possible two-photon transitions are being pictured in figure 3. When the electron energies are detected, electrons that went through a two-photon transition will be seen as sidebands in between the odd harmonics. If the IR intensity is kept sufficiently low transitions including more than two photons are so few that they will not significantly influence the result. As there are two quantum paths (one from a lower and one from a higher harmonic) to each sideband, these paths will interfere. The intensity of the sidebands will therefore be very sensitive to the phase difference between the IR and XUV fields. [7]

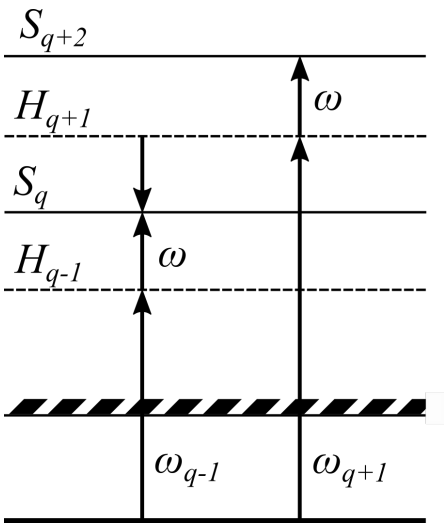

(a) The possible two-photon transitions to the sideband S_q.

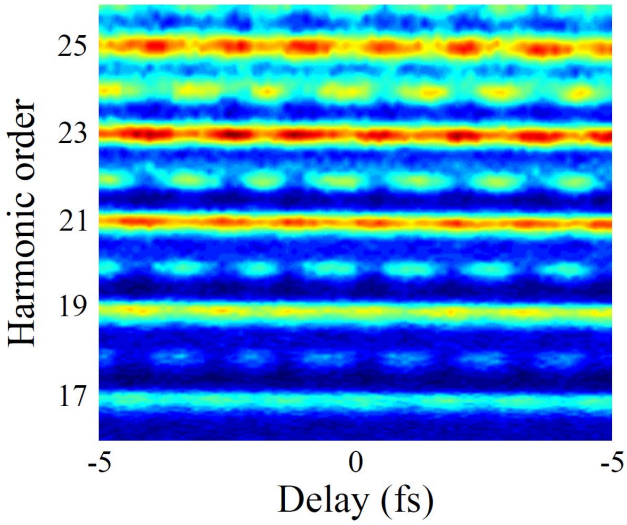

(b) A RABITT scan, showing harmonics 17 to 25. The sidebands appear as oscillating intensities in between the odd harmonics. The image is originally from [6].

Figure 3: In (a) is the possible paths to a sideband S_q visualized, and in (b) the sidebands, as they appear in a RABITT scan, is shown.

The scan is done by setting the delay τ between the IR and XUV fields to some arbitrary and unknown value τ_0 and detecting and counting electrons according to their kinetic energy at this point. The delay is then changed by a small known amount $\Delta\tau$, by shifting the difference in optical path length of the two arms of the interferometer. This is done by using a piezoelectric material to move one or more mirrors in the interferometer. The shift in delay $\Delta\tau(= \Delta d/c)$ can be related to a shift in phase (eq. 5). The detection of electrons is repeated at the new delay and the whole process is repeated until the complete scan is done. A typical result can be seen in figure 3 (b).

If it is assumed that only two-photon transitions contribute to the sidebands and that the amplitudes of the different quantum paths to the same sideband have equal amplitude, then the sideband intensity will change as

$$S_q(\tau) \propto 1 + cos(2\omega\tau - \Delta\phi_q - \Delta\phi_q^{at}),$$

where $\Delta\phi_q$ is the difference in phase between harmonic $q+1$ and harmonic $q-1$. $\Delta\phi_q^{at}$ is called the atomic phase and comes from the ionization process. It can in most cases be neglected. By fitting a sine function to the data of every sideband all $\Delta\phi_q$'s are obtained. The delay of all the harmonics is then calculated by an iterative process where the delay of the lowest order harmonic is assumed to be zero. The relative amplitudes of the harmonics can be directly obtained from the data. When both amplitude and delay, compared to the other harmonics, is known for all harmonics the entire attosecond pulse can be reconstructed.

3 Method

3.1 Error propagation in a sine function

To simulate the propagation of an error in the delay to an error in the fitted phase a MATLAB script that generates a number of data points $(\Delta\tau_i, I_i)$ and fits a sine function to these was constructed. The principle of generating data points with some error from an underlying function and fitting a curve to these points can be seen in figure 4. Each data point consists of a chosen delay $\Delta\tau_i$ and an intensity I_i. I_i is not the intensity at time $\Delta\tau_i$, but

$$I_i = Asin(f \cdot [\Delta\tau_i + \delta_\tau]) + I_0 - \delta_I,$$

where A is the amplitude, f is the frequency, δ_τ is a normally distributed error in time with mean zero, I_0 is the mean intensity, and δ_I is a stochastic error that is associated with measuring the intensity at the exact delay $[\Delta\tau_i + \delta_\tau]$. δ_I is assumed to be Poisson distributed with the square root of the actual intensity at $\Delta\tau = \Delta\tau_i + \delta_\tau$ as expectation value, *i. e.* $\lambda = \sqrt{Asin(f \cdot [\Delta\tau_i + \delta_\tau]) + I_0}$. The amplitude and mean intensity were both set to 1000. To each set of data points $\{(\Delta\tau_1, I_1), (\Delta\tau_2, I_2), ...,(\Delta\tau_n, I_n)\}$ a sine function,

$$g(x) = A_j sin(f_j \cdot [x + \phi_j]) + B_j,$$

is fitted, such that

$$\sum_{i=1}^{n} \big(I_i - g(\Delta\tau_i)\big)^2$$

is minimized. The process is repeated N times and the standard deviation for the error in the phase is calculated.

$$\sigma_\phi = \left(\frac{1}{N-1} \sum_{j=1}^{N} [\bar{\phi} - \phi_j]^2 \right)^{1/2},$$

where $\bar{\phi}$ is the mean of all the ϕ_j's.

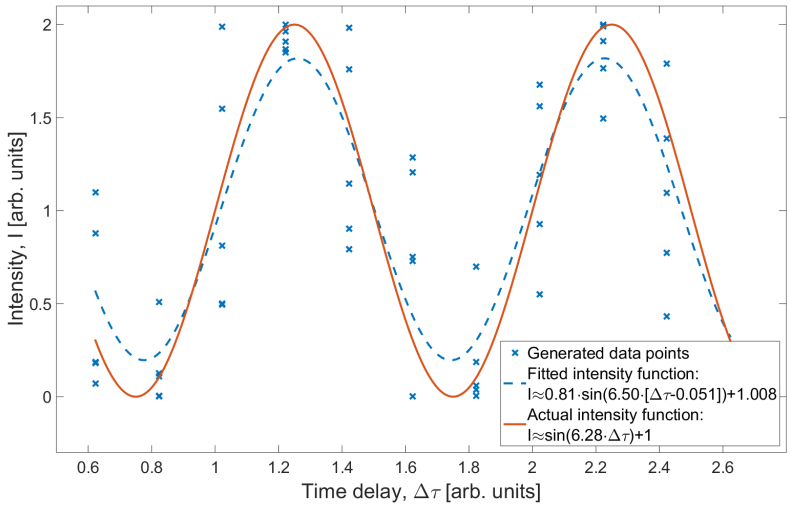

Figure 4: The dashed curve has been fitted to 50 data points, taken at 10 different delays, to try to find the phase of the solid curve. The standard deviation for the error in delay was 0.1 periods, *i. e.* $\sigma_{\Delta\tau} = 0.1T$.

To find out what sufficient stability means, this was tested for a few different cases, in which the number of delays (N_d), the standard deviation of the error in time ($\sigma_{\Delta\tau}$), the number of data points (n), and the number of periods sampled over (N_p) were varied. In total three runs were made. The results from these simulations are presented in section 4.2.

First the script was run for different number of delays, but with the total number of data points kept constant at 10 000. The number of periods sampled over was 10. For all the delays the number of iterations was 1000. The standard deviation of the error in delay was set to 0.05 periods, that is $\sigma_{\Delta\tau} = 0.05T$. The result of this can be found in figure 7.

In a second run the number of different delays was kept constant at 100, while the size of the time error and the total number of data points were varied. The number of periods sampled over was one and the number of iterations was 1000. In figure 8-9 the results from this run is plotted.

In a third run the number of periods sampled over was varied while the total number of data points was 10 000, the number of delays was 50, the number of iterations was 10 000, and the standard deviation of the error in the delay was $0.05T$. The result is shown in figure 10.

3.2 Stability of interferometers

To investigate the stability of different interferometer designs simulations of a laser moving relative to interferometers was performed in the ray tracing program FRED from Photon Engineering. Moving the laser simulates the movements that could arise when a setup, consisting of a laser source and an interferometer, is subject to vibrations. A completely random, but small, movement of the laser relative to the interferometer will lead to a combination of two effects: 1) the laser beam hits the interferometer at a new position, and 2)

the laser beam hits the interferometer at a different angle. These two effects were simulated individually by rotating the laser around the first element of the interferometer and by translating the laser perpendicular to the beam direction, respectively. Mostly movements in the horizontal plane (the plane in which y is constant) were considered. To standardize the process a stress test that consists of separate rotation and translation of the laser was constructed.

3.2.1 The stress test

In the stress test, spatial and temporal drift is measured for both translation and rotation of the laser. In total this gives four separate measures of stability. These are: (1) temporal drift due to rotation (as/degree), (2) spatial drift due to rotation (mm/degree), (3) temporal drift due to translation (as/mm), and (4) spatial drift due to translation (mm/mm).

The temporal drift is measured by observing fringes on a detector, which arises because of interference between the two arms of the interferometer. For the interference to become visible as fringes (and not merely as a change in the overall intensity) the recombination mirror was misaligned by a fraction of a degree. A typical interference pattern, as observed in FRED, is shown in figure 5 (b). The interferometer used to create the interference pattern is shown in figure 5 (a). As the laser is either rotated or translated to a new position the interference pattern at the detector is recorded and the phase of the dominating frequency is extracted, using a fast Fourier Transform. This is repeated at several angles/positions to obtain a number of data points that consists of a displacement (rotational or translational) and a phase. Using eq. 5 a corresponding delay is calculated for each phase, so that each data point consists of a displacement and a delay. The delay that corresponds to zero displacement is arbitrarily set to zero. A straight line is then fitted to these points to obtain a value, d_t, of how the temporal drift is related to either displacement.

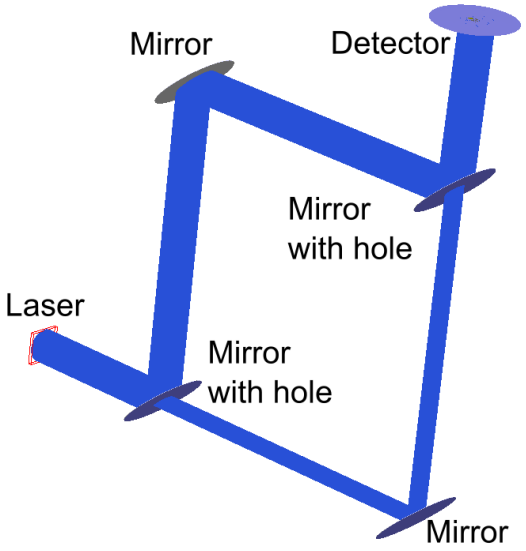

(a) A Mach–Zehnder interferometer, as seen in the ray tracing program FRED. This is the interferometer in figure 6 with $l_1 = l_2 = 100$.

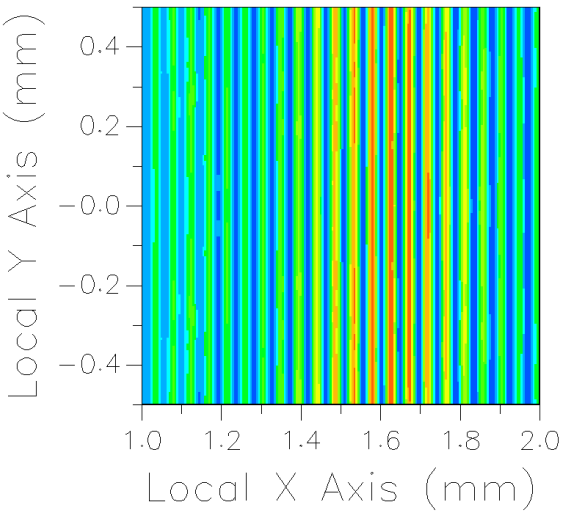

(b) This is what an interference pattern typically looks like in FRED. It was recorded using the interferometer in (a) and a detector with size 1 mm x 1 mm.

Figure 5: An interferometer and its associated interference pattern, as seen in FRED.

To measure the spatial drift a lens that focuses the recombined beams is installed and the position of each arm's best geometric focus before and after displacing the laser is recorded. By defining one vector, $\vec{v_1}$, as the vector that connects the two focuses before the displacement of the laser, another vector, $\vec{v_2}$, as the vector that connects the focuses after the displacement, and taking the norm of the difference between these vectors, a measure, d_s, of the spatial drift is obtained.

$$d_s = ||\vec{v_2} - \vec{v_1}||$$

The translational and rotational displacements that were used were 0.1 mm and 0.01 degrees.

3.2.2 The interferometer designs

The interferometer design that was used to test for the effect of different arm length, area and mirror misalignment can be seen in figure 6. It is a Mach–Zehnder interferometer, consisting of two ordinary mirrors and two mirrors with central circular holes, for splitting and recombination of the beam. Beam splitters could also have been used, but the interferometer that will be built will make use of holey mirrors, so therefore it is appropriate to use them in the simulations as well. By the use of mirrors with holes one gets an annular beam in one arm and a dot-like beam in the other arm. If the annular beam is used for HHG, then the remaining IR, in this arm, can easily be removed with a circular aperture, leaving the XUV untouched. This

is possible because the XUV will be produced in a small angle interval in the center of the annular IR beam, since the wave fronts in the focus will be planar. When testing different arm lengths l_1 and l_2 was kept equal, and when testing different areas ($A = l_1 \cdot l_2$) $l_1 + l_2$ was kept constant at 200 mm. The recombination mirror was misaligned by 0.5 degrees in both tests. When investigating the effect of mirror misalignment the arm lengths were kept equal ($l_1 = l_2 = 100\,\text{mm}$ while the misalignment angle, ψ, was varied.

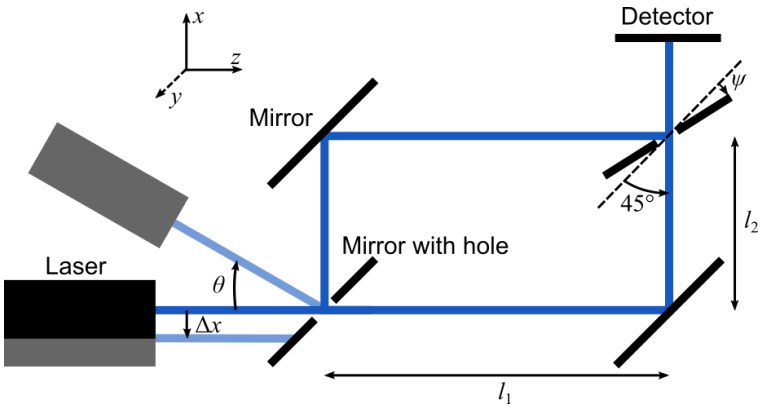

Figure 6: A schematic drawing of the simple Mach–Zehnder interferometer that was used to investigate how arm length, area and mirror misalignment influence stability.

The other parameters that were investigated are: mirror parity, lens parity, combined lens and mirror parity, and difference in focal length of lenses. The interferometers used for each parameter are all modifications of the interferometer in figure 6, and can be found in figure 19-22 in the appendix. As the effects of the combined lens and mirror parity was investigated, tests were performed not only with the laser moving in the horizontal plane (y is constant), but also with the laser rotating and translating in the vertical plane (x is constant).

When testing for equal lens parity, identical convex (focusing) lenses, each with focal length 50 mm, was inserted 150 mm before the recombination mirror in each arm. When the test was repeated for different lens parity, the convex lens in one of the arms was replaced by a concave lens of focal length -50 mm. The concave lens was placed 50 mm before the recombination mirror, so that its virtual focal point was at the same position as the focal point of the replaced convex lens. In the same way the position of the focal point was kept the same by changing the position of the lens, when different focal lengths were tested.

As a final step the exact same interferometer (the one in figure 6 with $l_1 = l_2 = 100$ mm and $\psi = 0.5°$) was tested for temporal drift with four different detector sizes (corresponding to 2, 5, 10, and 20 fringes). As the size of the detector does not have any influence on how the fringes move, but only on how they are observed, this was done to see if the observations done by the detector can be trusted.

4 Results and discussion

4.1 Sine error propagation

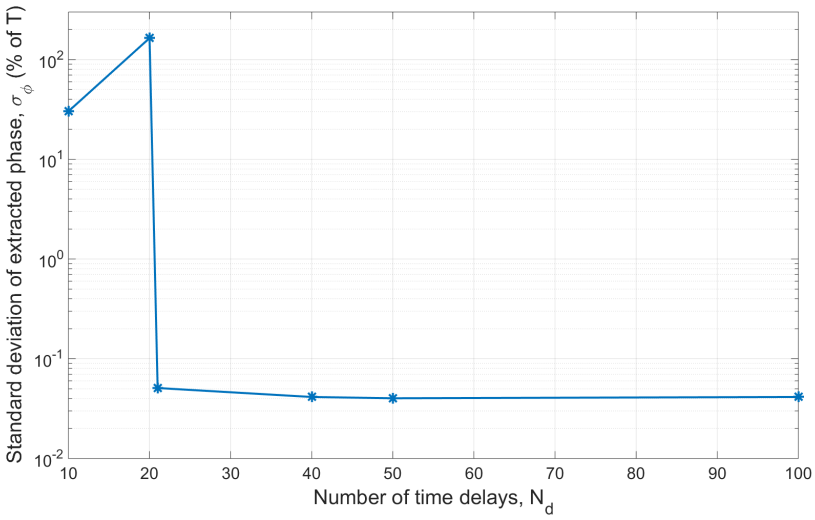

Figure 7: The standard deviations of the extracted phase, ϕ, of a sine function has been calculated from generated data points, as described in section 3.1, for different numbers of delays, N_d. The number of data points $n = 10000$, the number of iterations $N = 1000$, and the number of periods sampled over $N_p = 10$. For $N_d \leq 20$ the Nyquist criterion, which specifies the required sampling frequency, is not fulfilled, since the number of periods sampled over is 10.

In figure 7 the result of the first run, which is described in section 3.1, can be seen. The size of the error in the extracted phase has been plotted against the number of delays used. What stands out is the (more than) three orders of magnitude jump in the standard deviation of the extracted phase that occurs when increasing the number of sampling positions from 20 to 21. This is in accordance with the Nyquist criterion, which says that the sampling frequency must be greater than twice the frequency of the signal that is being sampled [8]. When the number of delays is 20 or less this criterion is not met, and therefore the phase that is being extracted is completely random. On the other hand, the standard deviation of the extracted phase becomes small as soon as the Nyquist criterion is fulfilled. Increasing the number of delays above the limit that is specified by the Nyquist criterion does not further decrease the standard deviation of the extracted phase by a significant amount.

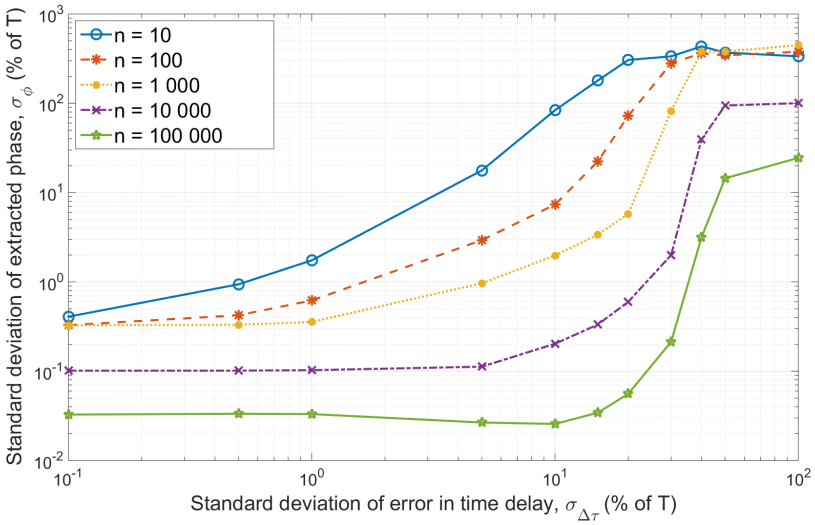

Figure 8: The standard deviations of the extracted phases has been calculated from generated data points, as described in section 3.1, for increasing errors in the delay. The different lines correspond to different numbers of generated data points. The number of iterations $N = 1000$, and the number of periods sampled over $N_p = 1$.

The result that is presented in figure 8 gives reason to point out three things. First of all, the error in the extracted phase decreases if the number of data points is increased. This is seen as an ordering of the lines according to the number of data points that they represent. Secondly, for the lines n=100 000, n=10 000 and n=1000, there are plateaus that extend up to approximately $\sigma_{\Delta\tau} = 0.1T$, $\sigma_{\Delta\tau} = 0.05T$ and $\sigma_{\Delta\tau} = 0.01T$, respectively. At each plateau the error in the extracted phase is basically constant, independently of the size of the error in the delay. This indicates that in these regions the error δ_I, associated with actually measuring the amplitude of the sine function, dominates over the error δ_τ, associated with measuring at the correct delay. What this means is that decreasing δ_τ has no effect in these regions. It is reasonable to assume that there are plateaus for n=10 and n=100 as well, but that these could not be resolved with the errors in the delays that were used. Thirdly, for each line (each number of data points) there is a transition region where the size of the error in the extracted phase changes by about three of orders of magnitude. As the number of data points is increased, this region is shifted towards higher values of $\sigma_{\Delta\tau}$ and becomes narrower.

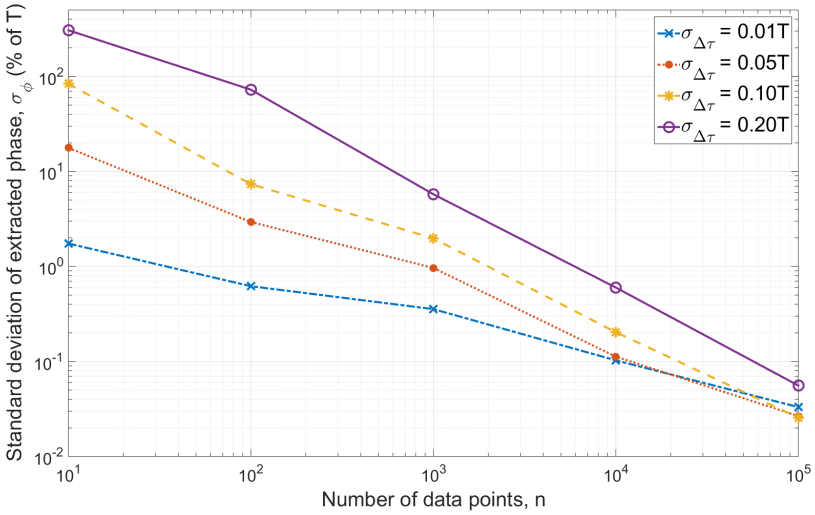

Figure 9: The standard deviations of the extracted phases has been calculated from generated data points, as described in section 3.1, for increasing number of data points. The different lines correspond to different standard deviations for the error in the delay. The number of iterations $N = 1000$, the number of delays $N_d = 10$, and the number of periods sampled over $N_p = 1$.

In figure 9 it can be seen that the standard deviation of the extracted phase decreases as the number of data points is increased. Since the lines converge as the number of data points is increased, it can also be concluded that the effect of the size of $\sigma_{\Delta\tau}$ on the size of σ_ϕ decreases as the number of data points is increased.

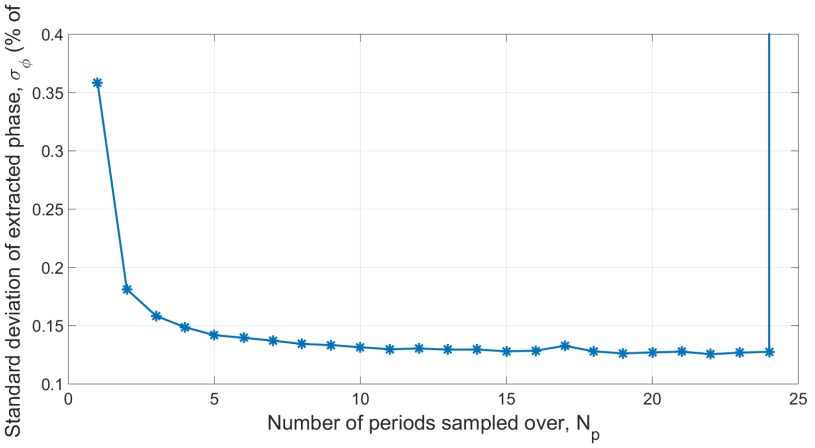

Figure 10: The standard deviations of the extracted phases has been calculated from generated data points, as described in section 3.1, sampled over an increasing number of periods. The number of iterations $N = 10000$, the number of data points $n = 10000$, the number of delays $N_d = 50$, and the standard deviation of the error in the delay $\sigma_{\Delta\tau} = 0.05T$. The last data point has been left out, since it is only of interest to conclude that σ_ϕ becomes large when $N_p \geq N_d/2$; the exact value is of minor interest.

The effect on the error in the extracted phase of changing the number of periods, N_p, over which the data points is sampled while keeping all other variables ($N, n, \sigma_{\Delta\tau}$ and N_d) constant is shown in figure 10. It is clear that the error in the extracted phase can be decreased by sampling over more than one period. In this case the error decreased by more than a factor two by increasing the number of periods from 1 to 5. The error does not continue to decrease infinitely as the number of periods is further increased, but remains at a fairly constant level all the way from 10 to 24 periods. At 25 periods the Nyquist criterion is no longer met (since $N_d = 50$) and extraction of the phase is therefore no longer meaningful, with a large σ_ϕ as a consequence.

4.2 Stability of interferometers

In this section a selection of the more interesting results will be presented and discussed. The complete results of the stability simulations can be found in the appendix in tables 1-9.

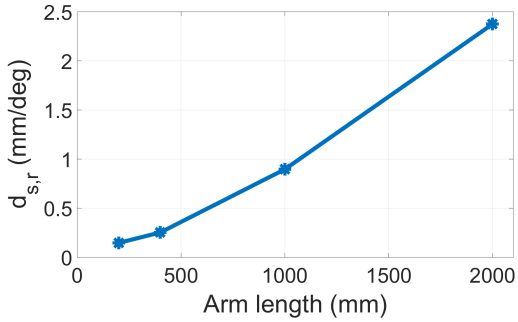

(a) Spatial drift due to rotation of the laser, $d_{s,r}$.

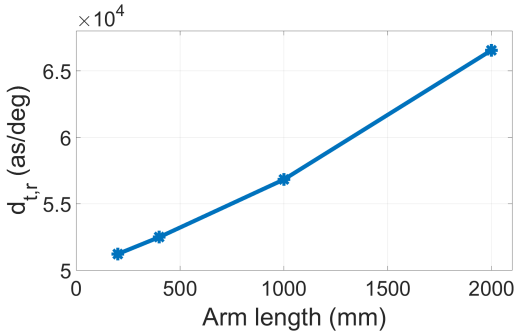

(b) Temporal drift due to rotation of the laser, $d_{t,r}$.

Figure 11: The spatial and temporal drift of, otherwise identical, interferometers of different arm lengths has been simulated as described in section 3.2.1.

In figure 11 two of the results from applying the stress test described in section 3.2.1 are presented. It is clear that when it comes to spatial and temporal drift due to rotation of the laser relative to the interferometer, it is better to have an interferometer with shorter arm length. There was no sign of the arm length influencing the spatial drift due to translation of the laser. This can be seen in table 1 in the appendix. In the same table is the result from measuring the temporal drift as an effect of translation. This result does not show any trend, but seem to be completely random. In section 4.3 it will be shown that this type of simulation (temporal drift due to translation) indeed gives results that can not be fully trusted, and they will therefore not be discussed in the following.

The second parameter of interferometer design that was investigated was area, *i. e.* the shape of an interferometer with constant arm length. There is no sign in the outcome (which can be found in table 2 in the appendix) of these simulations of the area influencing the temporal or the spatial drift. This does, however, not indicate that it is certain that the area of an interferometer is irrelevant for its stability. For example, these simulations do not take into account the possibility of the interferometer moving while the

laser pulse is inside it, something that could make the shape (and therefore the area) influence the stability.

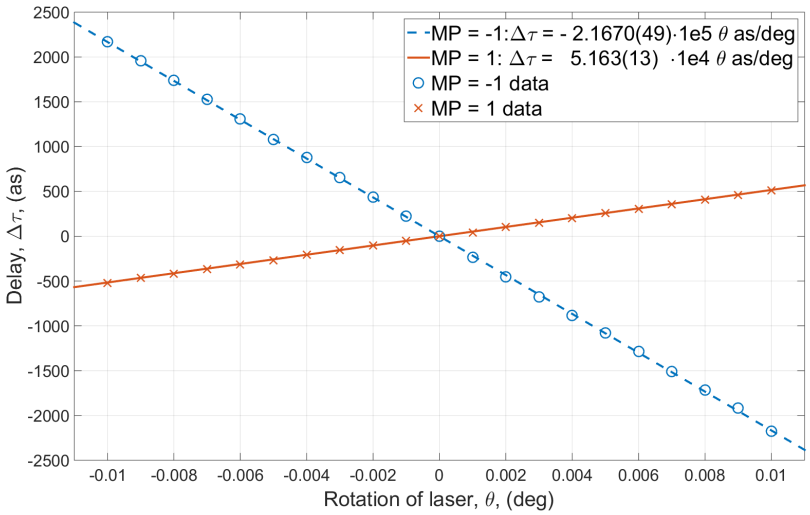

Figure 12: Simulations of the temporal drift due to rotation for interferometers with either different (MP = 1) or equal (MP = -1) mirror parity.

In figure 12 the temporal drift due to rotation for interferometers of either equal (MP = 1) or different mirror parity (MP = -1) is shown. Mirror parity is defined as

$$\text{MP} := (-1)^{m_1+m_2}, \tag{6}$$

where m_i is the number of mirrors in the i^{th} arm. In the legend of figure 14 the slopes of the lines in the figure are given. It can be seen that the delay of the interferometer with different mirror parities drifts approximately four ($|-2.2e5|/|5.2e4| \approx 4$) times faster than the interferometer with equal mirror parities. The spatial drift - both due to translation and rotation - of this interferometer is also greater than for the interferometer with equal mirror parities. This can be seen in table 3 in the appendix. For each mirror that is inserted in an interferometer arm, the laser beam will cross itself once, making the leftmost part of the beam the rightmost (and vice versa), as seen when looking in the direction of the beam. The crossing over will only occur in the plane that is perpendicular to the surface of the mirror and parallel to the direction of the beam. This means that if the first arm has an odd number of mirrors and the second an even number of mirrors, moving the laser to the right will make the first arm exit the interferometer more to the left, while the second arm will exit more to the right, *i. e.* the arms drift apart.

When the effect of lens parity was tested a convex lens was inserted in one of the arms and either a convex (same parity) or a concave (different parity) lens was inserted in the other arm. The drift of the interferometer with unequal lenses in its arms (LP = -1) turned out to be much larger than the drift of the interferometer with equal lenses in its arms (LP = 1). Both the spatial (due to either rotation or translation) and the temporal drift are almost three times larger. These results can be found in table 4 in the appendix.

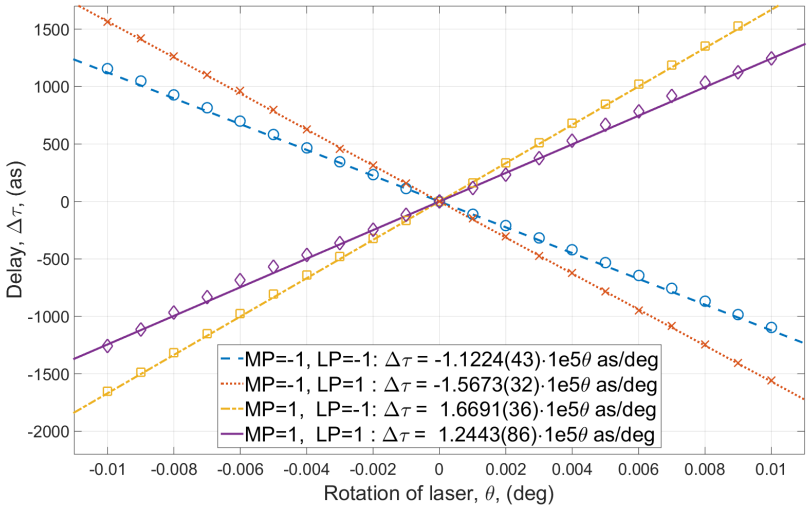

Figure 13: Simulations of the temporal drift due to rotation of the laser in the horizontal plane for interferometers with either equal (MP = LP) or different (MP $\neq$ LP) combined parity in the horizontal plane.

In figure 13 the combined effect of mirror parity and lens parity on temporal drift due to rotation is shown. The lens parity is defined in analogy with the mirror parity.

$$\text{LP} := (-1)^{\ell_1+\ell_2}, \tag{7}$$

where ℓ_i is the number of focusing lenses in the i^{th} arm. The lines with the least slopes are those that correspond to the mirror parity being equal to the lens parity. This shows that the important parameters are in fact not lens and mirror parity, but the combined parity. The problem with trying to balance a different mirror parity with a different lens parity is that lenses do not only make the laser beam cross itself in one plane, but in both planes parallel to the direction of the beam. This means that with LP = MP = -1 the total parities of the two arms can be equal in one plane, but different in another. The effect of this was investigated by rotating the laser in the vertical plane, and the result of this is shown in figure 14. The lines that correspond to the same (equal or different) lens parity are situated on top of each other. The results for spatial drift are similar. This verifies that the mirror parity does not influence how the arms drift due to vertical movements of the laser relative to the interferometer.

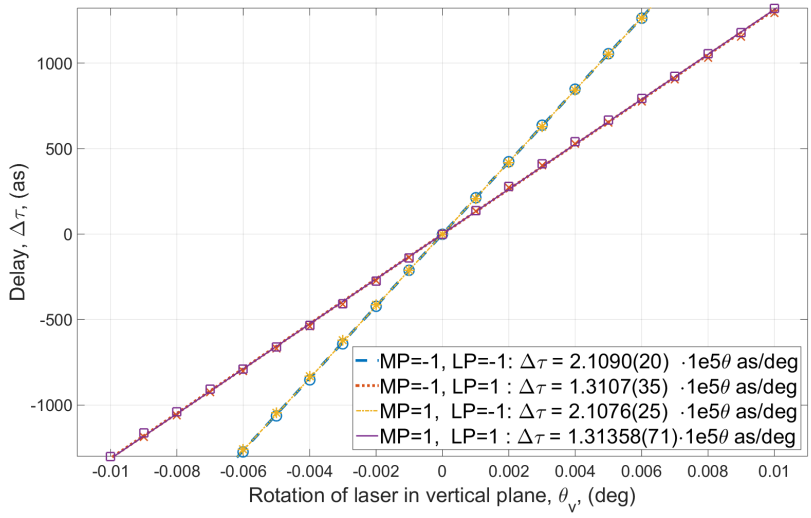

Figure 14: Simulations of the temporal drift due to rotation of the laser in the vertical plane for interferometers with either equal (MP = LP) or different (MP ≠ LP) combined parity in the horizontal plane.

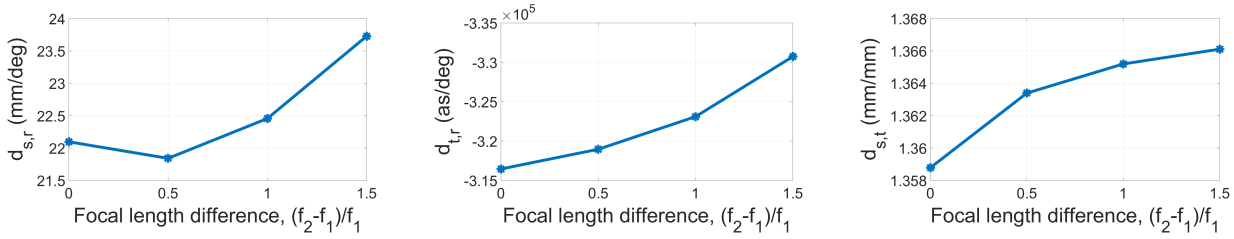

(a) Spatial drift due to rotation of the laser, $d_{s,r}$.

(b) Temporal drift due to rotation of the laser, $d_{t,r}$.

(c) Spatial drift due to translation of the laser, $d_{s,t}$.

Figure 15: The spatial and temporal drift of interferometers with lenses of increasing difference in focal length in the two arms. The simulations were performed as described in section 3.2.1.

In figure 15 (a-c) the results from applying the stress test on interferometers with increasing difference in focal length between the lenses in each arm, is presented. Except for the interferometer with a difference of 50 percent showing the least spatial drift due to rotation, it seems that the drift is less for interferometers with lenses with more similar focal lengths. The trend in figure 15 (b) and (c) is clear and unbroken, but in (a) there is an unexpected minimum. Still, even in (a) the general trend is that less difference in focal lengths leads to less drift.

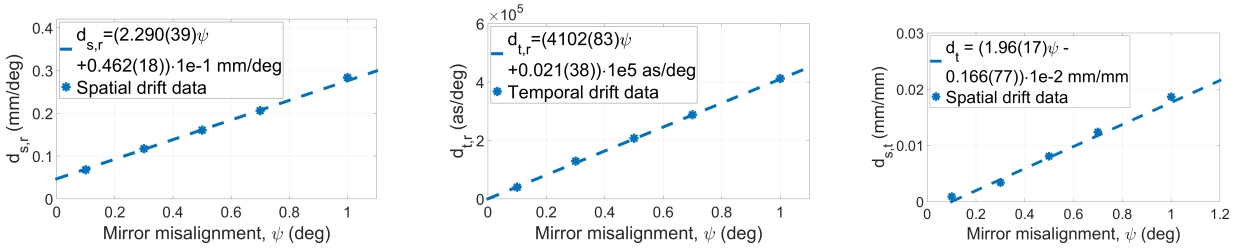

(a) Spatial drift due to rotation of the laser, $d_{s,r}$.

(b) Temporal drift due to rotation of the laser, $d_{t,r}$.

(c) Spatial drift due to translation of the laser, $d_{s,t}$.

Figure 16: The spatial and temporal drift of interferometers with one mirror being increasingly misaligned. The simulations were performed as described in section 3.2.1.

To see interference as fringes on the detector the beams that hit the detector have to have different incidence angles. To achieve this a mirror can be misaligned by some fraction of a degree. The more the mirror is misaligned, the more fringes will be visible on the detector. If the arms drift temporally compared to each other, the fringes will move. In the lab this is used to keep the interferometer stable. With the use of beam splitters a fraction of each arm is taken out and directed towards a screen. By misaligning one of the mirrors used to do this, fringes become visible on the screen. As soon as the fringes move a signal is sent to a delay stage, which in turn moves to counteract the drift. For this control system to work perfectly the drift in the control part of the interferometer must be equal to the drift in the main part of the interferometer. In figure 16 the result from applying the stress test on interferometers with increasingly misaligned mirrors is presented. What is seen is a linear relation between the degree of misalignment and the rate of the drift. The linear relation is present for both spatial and temporal drift due to rotation, and for spatial drift due to translation. What this means for the control system in the lab is that the drift seen on the control screen is greater than the drift in the part of the interferometer that is used for experiments. This would mean that the control system used to stabilize the interferometers in the lab is overcompensating.

4.3 The temporal drift simulations

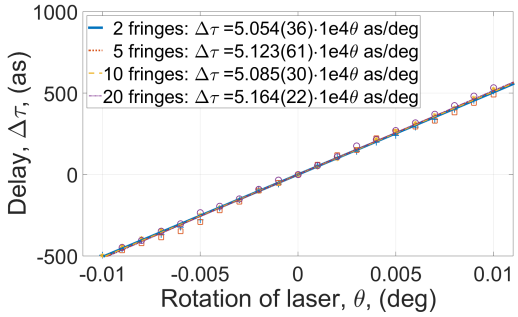

(a) Temporal drift due to rotation of the laser, $\dot{t}, r$.

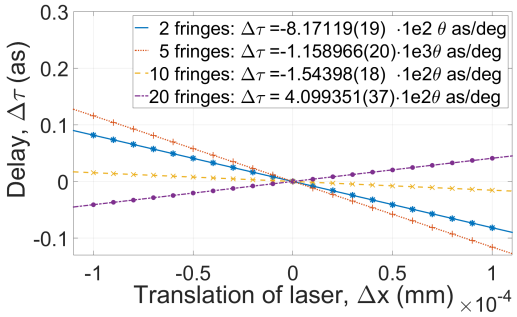

(b) Spatial drift due to translation of the laser, $\dot{t}, t$.

Figure 17: The temporal drift of identical interferometers due to rotation and translation of the laser. The only thing that separates the designs is the number of fringes that fit the detector.

In figure 17 (a) and (b), as well as in figure 12-14, it can be seen that the individual data points of a temporal drift simulation align along straight lines. This indicates that the data points are not random, but that they represent some real property of the interferometer being tested. If the size of the detector is being increased or decreased the slope of the line should remain constant, that is the relation between the amount the laser is being moved and the delay should not change. This is indeed the case when rotating the laser, as can be seen in figure 17 (a). For the different sized detectors, the difference between the maximum and minimum slope is just above 2 percent ((5.164-5.054)e4/5.054e4 $\approx 2.2\%$), which is an acceptable error margin for the purposes of this project. When translating the laser the result is completely different. This is seen in figure 17 (b). The data points still align along straight line, but the slopes of these lines differ in a seemingly random way. Therefore it is not possible to say that one interferometer design is more stable than another based on the outcome of a simulation of this type.

4.4 Considering the Rayleigh range

In an interferometer used for attosecond experiments it is important to have sufficiently long Rayleigh ranges at two focuses. The first is a focus in the gas-jet where HHG takes place. If the Rayleigh range is too short at this focus, there will be a large phase shift over the gas-jet, according to the Gouy effect (see section 2.1), and the generated XUV pulse will not be phase-locked to the IR. If the interferometer is built according to the conclusions of this project (see section 5), then there will be a lens of equal focal length in the second arm. The Rayleigh range of the corresponding focus will not matter, since no interaction takes place there. However, that focus could in certain experiments (such as RABITT) be imaged (by a focusing mirror outside of the interferometer) together with the focus of the first arm, onto another gas-jet, where the actual experiment takes place. This makes it important that the Rayleigh length of both the IR and the XUV is sufficiently long (to minimize the phase shift) at this focus. If the Rayleigh range of either the IR or

the XUV is short compared to the width of the gas-jet, the obtained data will have a lower contrast. In this case the limiting Rayleigh range will be that of the IR, since the XUV will have a small beam radius, and hence a long Rayleigh range. Since the IR part of this focus is an image of the focus of the second arm in the interferometer, the Rayleigh ranges of both focuses in the interferometer is of interest.

The laser beams used in the interferometers in this project are truncated due to passing holey mirrors and shutters and not truly Gaussian. Therefore eq. 3 can only be used to get an approximation of their Rayleigh ranges. With this in mind, the parameters that determine the Rayleigh range is: wavelength (λ), focal length (f), and beam radius (r). The wavelength can not be adjusted, but will be 1030 nm for the new laser. What could potentially be adjusted are the focal length and the beam radius. According to eq. 3 a long focal length and a small beam radius result in a longer Rayleigh range, which is what is wanted. However, a long focal length and a small beam radius would also mean that the minimum waist radius, W_0, increases (eq. 1 and 2), and as a direct consequence the intensity at the focus will decrease (since $I \propto W_0^{-2}$). If the intensity becomes too low, HHG will not be possible at the focus in question. Choosing the right focal length (and potentially beam radius) will therefore be a trade-off between a long Rayleigh range and a high intensity. Since the intensity of the new laser is not very high it is crucial to get this balance right, so that both intensity and Rayleigh range is sufficient at the focuses. The problem with having a short Rayleigh range is that the phase shift over the gas cell becomes large and this results in low contrast data. In figure 18 it is illustrated that over the same gas cell a beam with a shorter Rayleigh range will have larger phase shift than a beam with longer Rayleigh range.

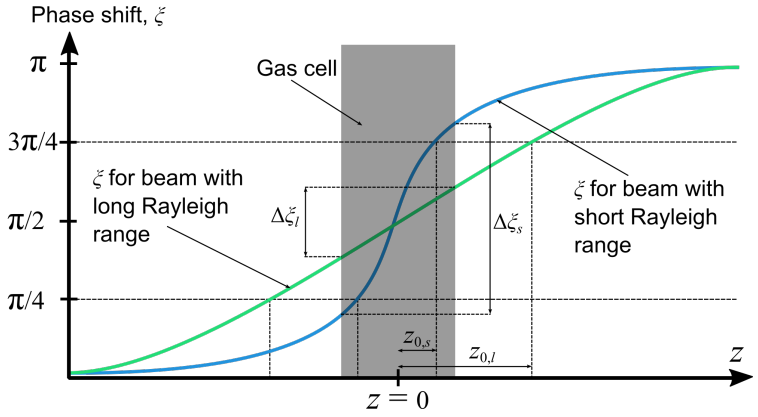

Figure 18: The beam with a long Rayleigh range has a smaller phase shift over the gas cell, compared to the beam with a shorter Rayleigh range. Half of the phase shift (from $\pi/4$ to $3\pi/4$) takes place within $\pm z_0$, therefore a longer Rayleigh range, z_0, leads to less phase shift within the gas cell.

The parameter that is decisive for the ability of the setup to produce data with high contrast is in reality not the Rayleigh range itself, but the ratio between the Rayleigh range and the width of the gas cell, where the interesting interaction takes place. Therefore a small gas cell means that the Rayleigh range can be shorter, without compromising the quality of the data. By letting the gas cell consist of nothing more than a

gas-jet nozzle, from which gas flows with high pressure into the beam focus, the inner diameter of the nozzle becomes decisive for the width of the gas cell. In an earlier experiment a laser, similar to the one that will be used for the new system, was used together with a gas-jet nozzle with an inner diameter of 90 μm and a focusing lens with 100 mm focal length for HHG. This setup yielded harmonics all the way up to the 77^{th} harmonic [9]. This effectively shows that HHG is feasible with this kind of laser, as long as the width of the gas cell is small and the focal length is short enough to allow sufficient intensity.

5 Conclusions

Using MATLAB the effects of an error in the delay was studied by error propagation simulations. How this error can be minimized was investigated by applying a stress test to different interferometer designs in the ray tracing program FRED.

The error propagation simulations were done by sampling data points with a random error from a sinusoidal function and extracting the phase of a sine function fitted to the data. The size of the error, the number of data points and the way the sampling were done were varied and the effect on the standard deviation of the extracted phase were recorded. It was found that even with a standard deviation of the error in the delay as large as $0.20T$, the standard deviation of the error in the extracted phase can be less than $0.001T$ if the number of data points is sufficiently large ($\approx$ 100 000). When the error in the delay was decreased, the error in the extracted phase only decreased to a certain level, where it remained fairly constant independently of the error in the delay. This indicates that it is not meaningful to strive to make the temporal drift of an interferometer zero (*i. e.* make the error in the delay zero), but only to get it below a certain level, as long as there is an uncertainty in the measurement itself. It was also found that, as long as Nyquist's criterion is fulfilled, the number of time delays in the sampling process is indifferent, and that it is better to sample over several, rather than few, periods.

To simulate how different choices in interferometer design affect the stability a stress test was constructed. In the stress test a laser was either translated or rotated relative to an interferometer, and the effect on spatial and temporal drift were measured. A high degree of drift would mean less stability. By varying one aspect of the design (such as arm length) at the time and observing how the rate of drift changed, conclusions about how an interferometer should be built to make it as stable as possible could be made. The parameters that were shown to result in a higher degree of stability was: 1) a shorter arm length, 2) equal parity of lenses and mirrors, 3) equal focal length of the lenses in each arm, and 4) no misalignment of the mirrors. For short: a stable interferometer is small and symmetric.

6 Outlook

In this section a few suggestions about what could be done with this project as a background is presented. These are: 1) to build an interferometer according to the principles outlined in the conclusions, 2) to inves-

tigate the effect of mirror misalignment on the control system of existing interferometers, and 3) to try to quantify how the parameters, that have been qualitatively investigated in this project, influence interferometer stability.

The most natural follow-up of this project would be to actually build an interferometer according to the principles that have been outlined. Such an interferometer has the potential to be very stable and could hence yield long data series of high quality. This would help further increasing the understanding of attophysics and potentially shed light on processes that take place in the attosecond timescale.

The results from this project indicate that the control system of the existing interferometers could in fact be overcompensating. Therefore investigating how the misalignment of a mirror in the control system actually affects precision of the control should be prioritized and could yield higher degree of stability already in the present setups. This could be done using simulations similar to those used in this project.

In this project only qualitatively statements about what aspects of interferometer design is better or worse when it comes to stability, is made. Future research could try to quantify these aspects, so that it would be possible to say by how much a particular choice in the design influences the stability. One way to do this would be to do more detailed simulations, where more complex stress is applied to the interferometers. Another, and more straightforward, way would be to build interferometers of different designs and measure their drift under real life conditions.

Acknowledgements

Foremost, I would like to express my sincere gratitude to my supervisor, senior researcher Johan Mauritsson, for excellent tutoring and encouragement. I would also like to direct a special thanks to my beloved wife, Hanna, for supporting me throughout this project.

References

[1] P. M. Paul *et al.* Observations of a train of attosecond pulses from high harmonic generation. *Science*, 292(5522):1689–1692, 2001.

[2] J. Mauritsson *et al.* Measurement and control of the frequency chirp rate of high-order harmonic pulses. *Physical Review A*, 70(2), 2004.

[3] B. E. A. Saleh M. C. Teich. *Fundamentals of Photonics.* Wiley, 2 edition, 2007.

[4] P. B. Corkum. Observations of a train of attosecond pulses from high harmonic generation. *Physical Review Letters*, 71(13):1994–1997, 1993.

[5] K. J. Schafer *et al.* Above threshold ionization beyond the high harmonic cutoff. *Physical Review Letters*, 70(13):1599–1602, 1993.

[6] K. Klünder. *Electron Wave Packet Dynamics on the Attosecond Time Scale*. PhD thesis, Lund University, 2012.

[7] H. G. Müller. Reconstruction of attosecond harmonic beating by interference of two-photon transitions. *Applied Physics B*, 74:17–21, 2002.

[8] H. Nyquist. Certain topics in telegraph transmission theory. *Transactions of the A. I. E. E.*, page 617–644, Feb. 1928.

[9] E. Lorek *et al.* High-order harmonic generation using a high-repetition-rate turnkey laser. *Review of Scientific Instruments*, 85(123106), 2014.

Appendix

Interferometers

Schematic drawings of the interferometers used when simulating the effect on stability of mirror parity, lens parity, the combination of lens and mirror parity, and difference in focal length between the lenses in each arm are presented in this section. The interferometer used for investigating the effect of arm length, area, mirror misalignment and detector size can be found in figure 6 in section 3.2.2.

Mirror parity, MP, and lens parity, LP, is defined in eq. 6 and eq. 6, respectively.

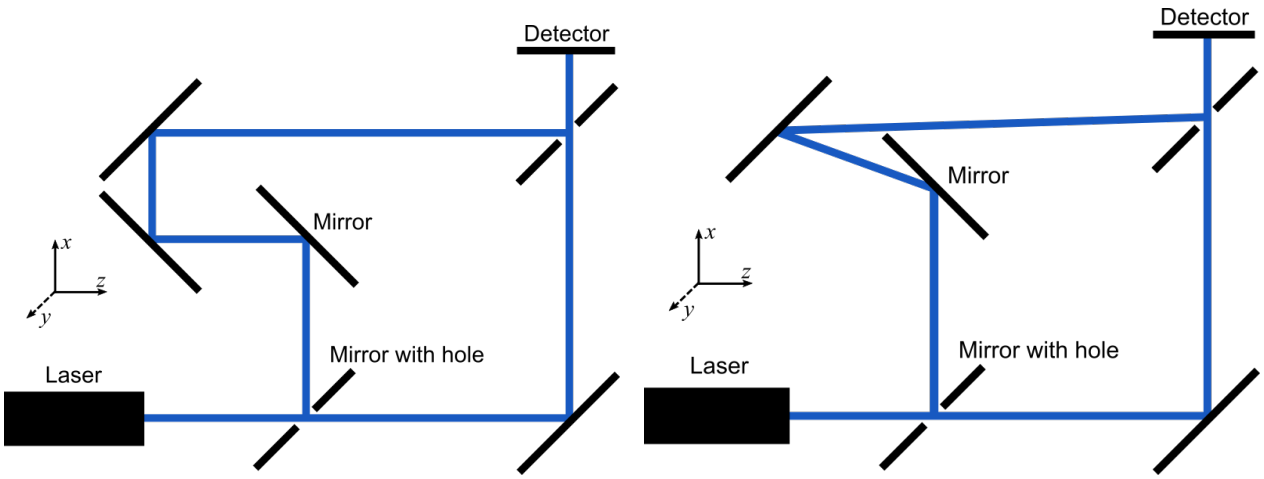

(a) MP = 1. **(b)** MP = -1.

Figure 19: The two interferometers used when investigating the effect of mirror parity on the stability of an interferometer.

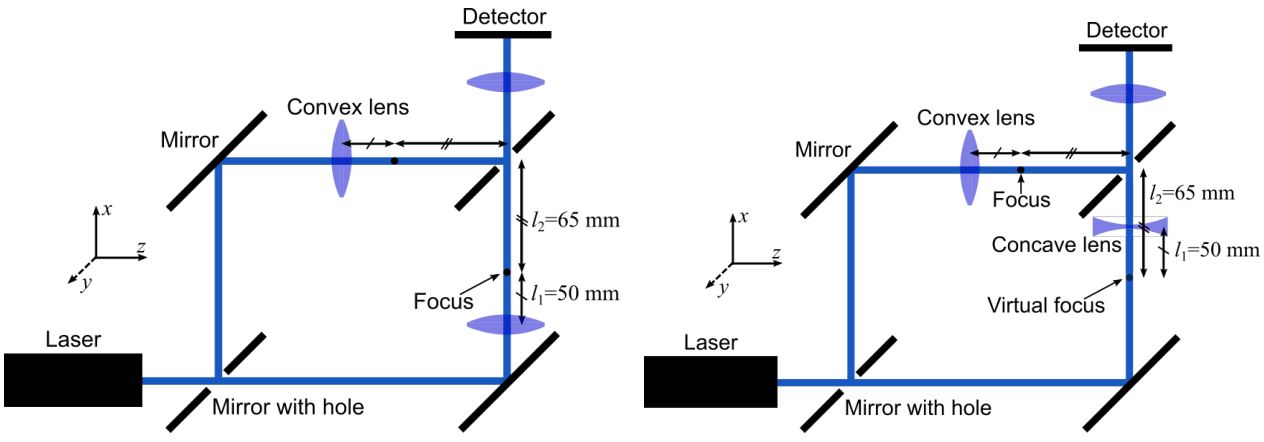

(a) LP = 1. **(b)** LP = -1.

Figure 20: The two interferometers used when investigating the effect of lens parity on the stability of an interferometer.

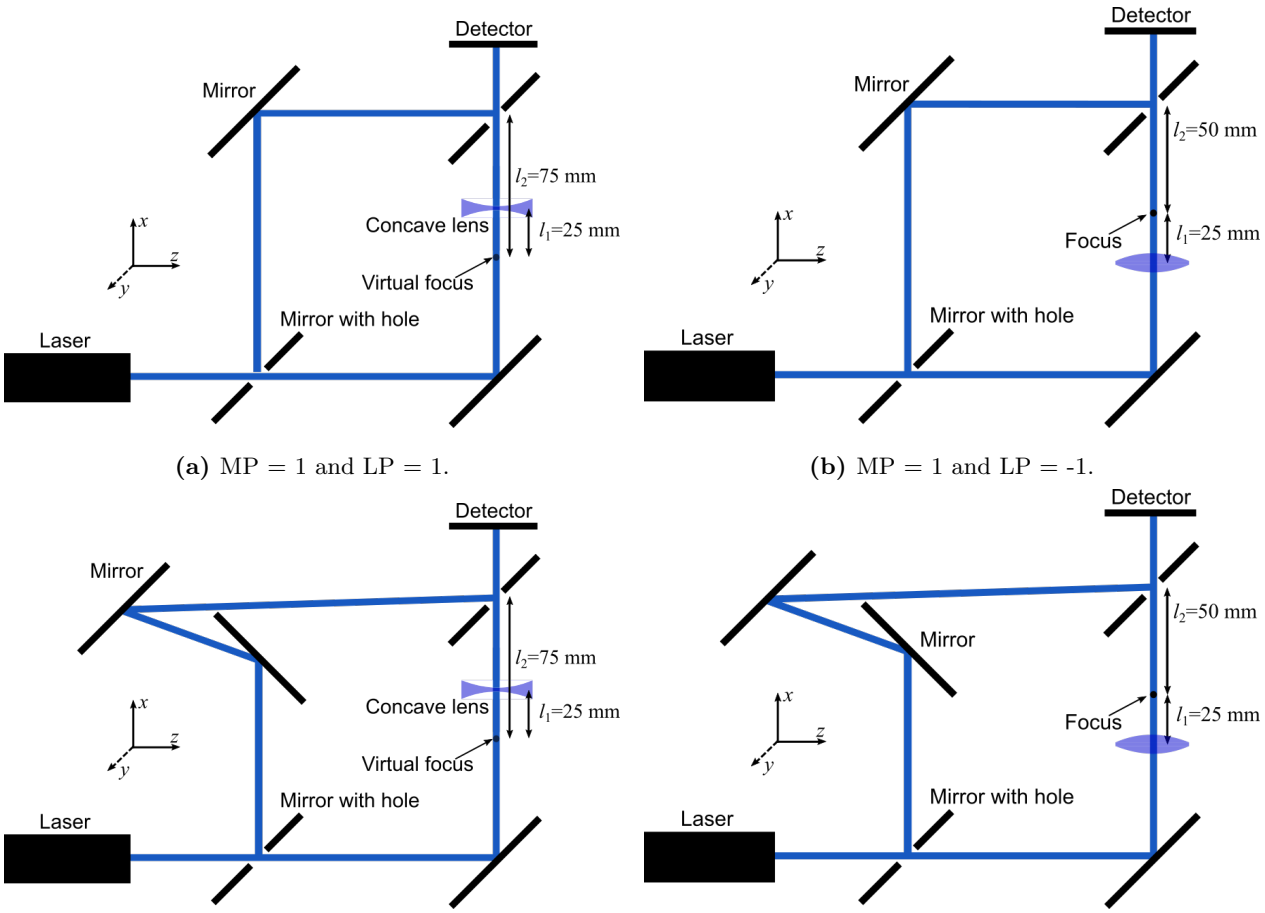

(a) MP = 1 and LP = 1.

(b) MP = 1 and LP = -1.

(c) MP = -1 and LP = 1.

(d) MP = 1 and LP = -1.

Figure 21: The four interferometers used when investigating the combined effect of mirror and lens parity on the stability of an interferometer.

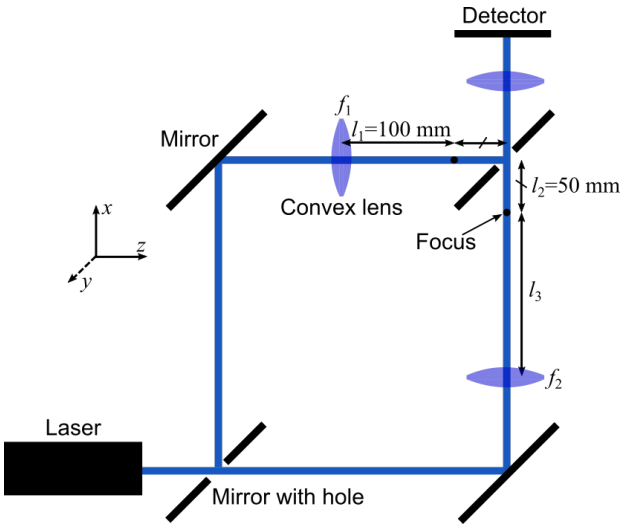

Figure 22: The interferometer used when investigating the effect of difference in focal length on the stability of an interferometer. The focal length $f_2 = l_3$ were varied, while $f_1 = l_1$ were kept constant, to see how the stability changed for different focal lengths.

Results

In this section the complete results from the stability simulations are presented. In all tables $d_{s,r}$ = [spatial drift due to rotation], $d_{t,r}$ = [temporal drift due to rotation], $d_{s,t}$ = [spatial drift due to translation], and $d_{t,t}$ = [temporal drift due to translation].

Table 1: The effect of arm length on spatial and temporal drift.

Arm length	$d_{s,r}$ **(mm/deg)**	$d_{t,r}$ **(as/deg)**	$d_{s,t}$ **(mm/mm)**	$d_{t,t}$ **(as/mm)**
200 mm	1.4708E-01	5.1226E+04	7.5053E-03	3.3682E+02
400 mm	2.5300E-01	5.2496E+04	7.5053E-03	2.9289E+02
1000 mm	8.9645E-01	5.6829E+04	7.5053E-03	2.1268E+02
2000 mm	2.3746E+00	6.6554E+04	7.5053E-03	3.0802E+02

Table 2: The effect of area on spatial and temporal drift.

Area	$d_{s,r}$ **(mm/deg)**	$d_{t,r}$ **(as/deg)**	$d_{s,t}$ **(mm/mm)**	$d_{t,t}$ **(as/mm)**
3600 mm^2	1.5059E-01	5.1275E+04	7.5053E-03	3.5947E+02
7500 mm^2	1.4708E-01	5.1305E+04	7.5053E-03	3.5947E+02
10000 mm^2	1.4708E-01	5.1226E+04	7.5053E-03	3.3682E+02

Table 3: The effect of mirror parity on spatial and temporal drift.

Mirror parity	$d_{s,r}$ **(mm/deg)**	$d_{t,r}$ **(as/deg)**	$d_{s,t}$ **(mm/mm)**	$d_{t,t}$ **(as/mm)**
MP = 1	1.7801E-01	5.1634E+04	7.5053E-03	3.4760E+02
MP = -1	3.5211E+00	-2.1670E+05	1.3761E-02	1.7881E+02

Table 4: The effect of lens parity on spatial and temporal drift.

Lens parity	$d_{s,r}$ **(mm/deg)**	$d_{t,r}$ **(as/deg)**	$d_{s,t}$ **(mm/mm)**	$d_{t,t}$ **(as/mm)**
LP = 1	3.2483E+00	-7.3690E+04	2.6897E-01	1.7869E+02
LP = -1	9.0484E+00	-2.0604E+05	7.3980E-01	-3.5413E+02

Table 5: The effect of combined lens and mirror on spatial and temporal drift, when moving the laser in the horizontal plane.

Combined parity, horizontal	$d_{s,r}$ **(mm/deg)**	$d_{t,r}$ **(as/deg)**	$d_{s,t}$ **(mm/mm)**	$d_{t,t}$ **(as/mm)**
MP = -1, LP = -1	7.1075E-01	-1.1224E+05	7.2491E-02	2.8265E+02
MP = -1, LP = 1	1.4021E+00	-1.5673E+05	5.6724E-02	1.3837E+03
MP = 1, LP = -1	1.4486E+00	1.6691E+05	5.2467E-02	1.3902E+03
MP = 1, LP = 1	7.5690E-01	1.2443E+05	6.8226E-02	5.9917E+02

Table 6: The effect of combined lens and mirror on spatial and temporal drift, when moving the laser in the vertical plane.

Combined parity, vertical	$d_{s,r}$ **(mm/deg)**	$d_{t,r}$ **(as/deg)**	$d_{s,t}$ **(mm/mm)**	$d_{t,t}$ **(as/mm)**
MP = -1, LP = -1	9.4667E-01	2.1089E+05	5.1253E-02	-6.4380E+02
MP = -1, LP = 1	3.2369E-01	1.3152E+05	4.9237E-02	-2.2567E+02
MP = 1, LP = -1	9.4232E-01	2.1071E+05	5.5226E-02	-5.4172E+02
MP = 1, LP = 1	3.2266E-01	1.3136E+05	4.9237E-02	-6.2666E+01

Table 7: The effect of difference in focal length for focusing lenses between the two arms on spatial and temporal drift.

Difference in focal length $(f_2 - f_1)/f_1)$	$d_{s,r}$ **(mm/deg)**	$d_{t,r}$ **(as/deg)**	$d_{s,t}$ **(mm/mm)**	$d_{t,t}$ **(as/mm)**
0.0	2.2096E+01	-3.1645E+05	1.3588E+00	1.7245E+02
0.5	2.1841E+01	-3.1895E+05	1.3634E+00	4.7161E+02
1.0	2.2456E+01	-3.2310E+05	1.3652E+00	1.3338E+02
1.5	2.3728E+01	-3.3073E+05	1.3661E+00	2.5455E+02

Table 8: The effect of mirror misalignment on spatial and temporal drift.

Mirror misalignment	$d_{s,r}$ **(mm/deg)**	$d_{t,r}$ **(as/deg)**	$d_{s,t}$ **(mm/mm)**	$d_{t,t}$ **(as/mm)**
0.1°	6.7788E-02	4.0293E+04	8.7440E-04	9.7242E+02
0.3°	1.1692E-01	1.2932E+05	3.3947E-03	-1.3437E+02
0.5°	1.6040E-01	2.0727E+05	8.0493E-03	-1.8698E+02
0.7°	2.0598E-01	2.8777E+05	1.2379E-02	-5.4103E+02
1.0°	2.8303E-01	4.1188E+05	1.8639E-02	-6.0831E+00

Table 9: The effect of detector size on temporal drift. The size of the detectors is represented by the number of fringes that fit the detector.

Detector size	$d_{t,r}$ **(as/deg)**	$d_{t,t}$ **(as/mm)**
2 fringes	5.0537E+04	-8.1712E+02
5 fringes	5.1233E+04	-1.1590E+03
10 fringes	5.0854E+04	-1.5440E+02
20 fringes	5.1643E+04	4.0994E+02